Contents lists available at ScienceDirect

Surface & Coatings Technology

journal homepage: www.elsevier.com/locate/sct

Full length article

Pulsed laser deposition of (TaNbHfTiZr)C high-entropy carbide layers with 38 GPa hardness

Tadeus Nikos Hogenelst [a,b], Cyrian Leriche [a,b,1], Alessandro Troglia [a,2], Bart Weber [a,b], Roland Bliem [a,b,*]

[a] Advanced Research Center for Nanolithography, Science Park 106, Amsterdam, 1098 XG, The Netherlands
[b] van der Waals-Zeeman Institute, Institute of Physics, University of Amsterdam, Science Park 904, Amsterdam, 1098 XH, The Netherlands

ARTICLE INFO

Keywords:
Hard coatings
Pulsed laser deposition
Carbide
High-entropy materials
Ceramics

ABSTRACT

High-entropy carbides (HECs) have been identified as high performance materials with attractive properties including superior penetration hardness in comparison to binary carbides. Traditional fabrication techniques for HEC materials often focus on creating bulk material with limited tunability. The growth of HEC coatings with the versatile thin-film growth method pulsed laser deposition (PLD), however, remains unexplored. Here, we fabricate thin films of the refractory high-entropy carbide (TaNbHfTiZr)C on $Al_2O_3(0001)$ and Si(100) substrates using PLD. PLD allows to optimize the composition and structure of the HEC layers to achieve single-phase, oriented carbide layers via systematic variations of the laser fluence, inert gas background pressure, and deposition temperature. Upon growth at room temperature, the carbide is found to coexist with a secondary phase of elemental carbon, which likely acts as embedding layer for carbide particles. The surface content of elemental carbon drops strongly when increasing the Ne background pressure while the carbon attributed to the carbide lattice responds less to pressure. At high growth temperatures (850 °C), little to no elemental carbon is observed and the carbide phase shows a significantly smaller carbon deficiency ($MC_{0.92}$). This change in composition is concomitant with an increased crystallinity and the emergence of an orientational preference with respect to the $Al_2O_3(0001)$ substrate. The layers with optimized crystallinity (ultra-high vacuum, 850 °C) achieve a hardness of 38.3 ± 1.9 GPa, which is close to the highest bulk values for HECs and demonstrates the promise of PLD-grown HECs for hard coatings.

1. Introduction

Refractory metal carbides (RMCs) are known for excellent mechanical, thermal, and chemical stability [1–4] and are hence common materials for applications at extreme temperatures, mechanical stresses and in corrosive environments. Such applications include tribological surfaces [5], corrosion-resistant materials [6], and hard coatings for mechanical processing [7]. RMCs are versatile materials with a wide range of properties thanks to the compatibility of the carbide lattice with different refractory metals and a wide range of carbon stoichiometries. The metal content strongly affects the material properties, both via the choice of refractory material as well as the alloying fraction of the constituent metals, which allows for engineering of application-oriented properties including the hardness [8,9] or heat conduction [10]. Close to the nominal composition, deviations in carbon content reflect the anion lattice vacancy concentration [11–14], which influences properties such as their thermal conductivity [15]. Further tuning of macroscopic material properties is possible via the microstructure of RMCs, for example if a variable degree of embedding into amorphous carbon is achieved as function of growth conditions, which for example allows for lattice parameter engineering [16].

In the case of multi-elemental carbides, there is ample opportunity to fine-tune material properties via the composition of the metal sublattice. These multi-elemental RMCs, however, can be metastable with respect to demixing and phase decomposition [17]. A large number of principal constituents [18,19], on the other hand, also increases the configurational entropy of the mixture [19], which can lead to the formation of a single phase. The resulting high-entropy carbides (HECs) have been reported to show an improved phase stability [18–22] and to exhibit enhanced hardness and corrosion resistance compared to simpler compositions [3,18,20]. The refractory HEC (TaNbHfTiZr)C

---

[*] Corresponding author at: Advanced Research Center for Nanolithography, Science Park 106, Amsterdam, 1098 XG, The Netherlands.
E-mail address: r.bliem@arcnl.nl (R. Bliem).

[1] Present address: University of Pennsylvania, 3451 Walnut Street, Philadelphia, PA, 19104, United States

[2] Present address: TNO, Stieltjesweg 1, 2628 CK Delft, The Netherlands

https://doi.org/10.1016/j.surfcoat.2025.132976
Received 12 September 2025; Received in revised form 27 October 2025; Accepted 18 November 2025

provides a good example of a material with entropy-enhanced properties and phase stability [3,18,23]. This material has been studied for example for its high hardness [20,23–26], wear-resistance [27], compressive strength [28,29], thermal stability [25,28], and corrosion resistance [30].

Several of these properties make (TaNbHfTiZr)C and other HECs promising materials for functional coatings. However, fabrication techniques that have been explored thus far focused mostly on bulk synthesis [20,21,23,26–28,30]. Nanohardness values up to 40.6 GPa were achieved for hot press sintering [26], while 32 GPa [20,23] and 38.5–39.5 GPa [27] have been reported for spark plasma sintering. Coatings were produced using sputter deposition, but they achieved inferior hardness values of 27.5 GPa [24] and 24 GPa [31]. Indeed the variation of the material properties between individual preparations of bulk (TaNbHfTiZr)C demonstrate the versatility of the material but also emphasize the importance of well-defined stoichiometry transfer during deposition and the ability to fine-tune the properties via growth parameters. These challenges can be addressed by versatile thin-film growth methods, such as pulsed laser deposition (PLD). PLD offers several advantages for growing compositionally complex materials, for example control over target stoichiometry, influence on composition via the choice of background gas, tunability of structure, and clean deposition environment and has been applied to grow simpler carbides [1,32,33] and several types of high-entropy materials [34–38] but no HECs.

Here, we demonstrate that PLD can provide good stoichiometry transfer and a high level of control over the growth of single-phase (TaNbHfTiZr)C thin films. We report trends in the surface composition and structure of the resulting films as a function of the PLD parameters laser fluence, deposition pressure and substrate temperature. For the coatings with the highest levels of crystallinity and orientational preference, we observe hardness values that are among the highest values reported for this carbide, showing the importance of control over growth for the application of HECs such as (TaNbHfTiZr)C as hard coatings. Our findings open new avenues for the application of high-performance HEC thin film coatings, for example in the semiconductor industry where high hardness and low wear are desirable for precision positioning.

2. Experimental

Pulsed laser deposition — (TaNbHfTiZr)C thin films were deposited onto 5 × 5 mm^2 Si(100) and $Al_2O_3(0001)$ substrates by PLD. A KrF excimer laser (λ = 248 nm, τ_p = 20 ns) with homogeneous energy distribution (flat-top profile) was used to ablate a stoichiometric hot-pressed target (HfC:NbC:TaC:TiC:ZrC 99.95 wt%). The composition gradient of the deposition target is assumed to be smaller than the ablation spot area $A_{target} = 1\ \mathrm{mm} \times 0.4\ \mathrm{mm}$. To minimize the influence of ablation residue, the deposition target was regularly re-prepared by wire spark erosion. Before every film growth, the target was prepared by pre-ablation in an Ar atmosphere. The depositions were performed in UHV ($p_{max} < 10^{-9}$ mbar) and in Ne background pressures ranging from 10^{-3} mbar to 3×10^{-2} mbar. Higher pressures were tested but resulted in high levels of oxygen contamination and oxide formation in the surface region. To estimate a layer thickness, the deposition rate was calibrated using a mechanical profilometer scanning over a sharp edge on a layer of (TaNbHfTiZr)C/$Al_2O_3(0001)$ deposited at F = 11 J/cm^2 and in 10^{-2} mbar Ne, yielding 50 nm ± 3 nm for 12 000 shots and thus an estimated growth rate of r_{Ne} = 0.004167 nm/pulse. The samples for the study of the effect of growth parameters were grown using 18 000 shots (≈75 nm), with the exception of the UHV reference samples (4500 shots ≈20 nm) and the fluence-dependent study with a larger variation of 1800 to 7500 pulses, corresponding to a thickness estimate of 7.5–30 nm. Due to the requirement of higher thickness for nanoindentation, a thicker layer with 144 000 shots (≈600 nm) in UHV was grown for the hardness measurement. The thickness estimate is valid for samples grown at identical PLD parameters as in the thickness calibration and holds only approximately true for other growth conditions. For depositions at high temperature, an infrared laser heater (λ = 980 nm) was used to set the substrate temperature T_s, which was measured by two-color Sensotherm M322 pyrometer aimed directly at the substrate surface.

Sample preparation — Si(100) with native SiO_x layer was chosen as substrate for disordered growth of (TaNbHfTiZr)C and sapphire $Al_2O_3(0001)$ for growth with an orientational preference, based on reports on the epitaxial growth of cubic metal carbides on $Al_2O_3(0001)$ [39]. The high-temperature depositions were exclusively performed on $Al_2O_3(0001)$ because Si interdiffusion was observed on Si substrates. The substrates were prepared for UHV by ultrasonication in acetone and isopropyl alcohol.

X-ray photoelectron spectroscopy — The surface composition of (TaNbHfTiZr)C was measured with x-ray photoelectron spectroscopy (XPS). As-deposited films were transferred to the XPS measurement chamber in UHV without breaking vacuum. Samples were excited with a monochromated Al-Kα x-ray source (1486.6 eV). XPS spectra were acquired by a Scienta Omicron R4000 HiPP-3 analyzer (swift acceleration mode, entrance slit 1 mm). Survey spectra were acquired at a pass energy (PE) of 500 eV, detailed spectra at a PE of 300 eV and 500 eV. XPS data was processed with the fitting software KolXPD using a Shirley background [40] and Voigt lineshapes for the individual peaks. All survey spectra were checked for Si 2*p* or Al 2*p* XPS intensity to rule out major dewetting exposing patches of substrate material.

Grazing-incidence X-ray diffraction — The structure of the (TaNbHfTiZr)C films was measured *ex situ* by grazing-incidence x-ray diffraction (GIXRD) using a Bruker D8 QUEST diffractometer with an Incoatec IμS 3.0 Cu Kα x-ray source ($\lambda = 1.5406$ Å). A PHOTON II Charge-integrating Pixel Array Detector was used to spatially resolve the two-dimensional diffraction patterns. The grazing angle was optimized by minimizing the substrate diffraction peaks for each sample. The experimental background was subtracted with IGOR PRO using a double exponential fit. Residual shifts of 1–2° of the absolute peak positions cannot be excluded based on sample tilt and three-dimensional specimen displacement errors going beyond the z-correction that has been applied. The diffraction results thus provide reliable information on the type of structure and the peak width of the peaks but are not used to determine lattice constants. For particle size calculations the 1D integrated GIXRD data was fitted with Voigt functions, which converged to have almost exclusively Lorentzian components, except for the peak corresponding to the (111) plane, for which Gaussian and Lorentzian component become comparable for the samples grown at low temperature. The grain sizes of the films are calculated using the Scherrer equation, in a coarse approximation attributing the full broadening to size effects and thus assuming a negligible contribution from strain and instrumental broadening. Given the absence of information on the shape of the particles, a common choice of shape factor of $K = 0.9$ was used [41].

Electron microscopy — The surfaces of the carbide layers were imaged using an FEI Verios 460 scanning electron microscope, operated at sample landing energies between 5 keV and 10 keV.

Nanoindentation — The hardness of an approximately 600 nm thick layer of (TaNbHfTiZr)C grown onto $Al_2O_3(0001)$ in UHV at 850 °C was measured by nanoindentation using a FemtoTools FT-I04 nanoindenter equipped with a Berkovich diamond tip (radius ≈ 200 nm) attached to an FT-200000 uniaxial microelectromechanical system (MEMS) force sensor. The indentations were performed using Continuous Stiffness Measurement (CSM) mode [42] at 2 nm amplitude and 200 Hz oscillation frequency allowing for computation of material properties including hardness as a function of indentation depth. This process generates a force-distance curve as a series of small-range force-distance curves for each CSM oscillation, in which the initial points of unloading represent the material's local elastic response [42]. The initial approach speed was set at 100 nm/s before contact, and set to 5 nm/s after

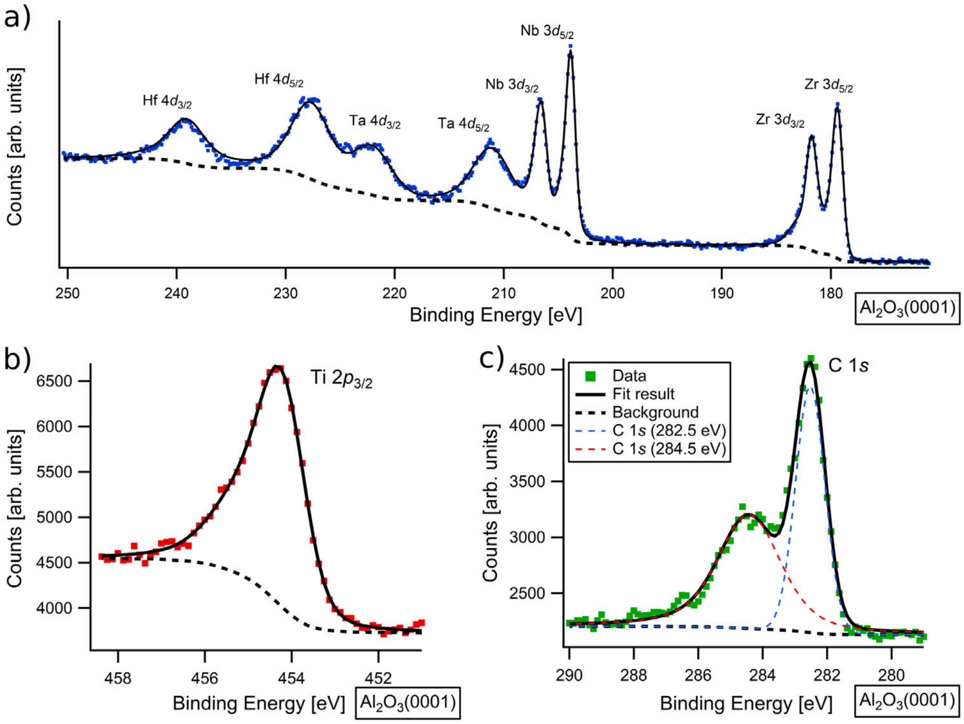

Fig. 1. UHV-XPS regions of as-deposited (TaNbHfTiZr)C deposited onto $Al_2O_3(0001)$ at F = 10 J cm^{-2} for 18 000 shots in 10^{-3} mbar Ne. The regions displayed serve as an indicator of the regions used for quantitative analysis of metal and carbon content. The Hf 4*d*, Ta 4*d*, Nb 3*d* and Zr 3*d* (a), the Ti $2p_{3/2}$ (b) and C 1*s* (c) transitions are used for quantification. For the carbon content two species are fitted corresponding to carbon–carbon bonds (284.5 eV) and carbon-metal bonds (282.5 eV).

contact. The total indentation depth was set at 450 nm. The Olivier-Pharr model [43] was used to calculate the tip contact area and true indentation depth, using the tip's geometry and measured stiffness response as input parameters. The hardness data was acquired in 25 individual measurements performed over a grid of 50 μm^2 and averaged by selecting a 1 nm depth bin size (N_{avg} = 350 per bin). The local hardness values (H) were calculated for each point by dividing the applied load by the total contact area. Before any calibration or hardness measurement performed, the Berkovich tip was cleaned by indentation into a piece of Cu. An initial calibration measurement was performed an $Al_2O_3(0001)$ substrate from the same diced wafer as the substrates used for deposition. After calibration, the stiffness responses of the sample and substrate were measured separately [42–44]. The statistics were calculated after filtering measurement artefacts (zeroes, negative hardness and tip retraction artefacts) from the data. The total data set was pooled into bins of 1 nm contact depth, establishing a mean hardness and standard deviation for each 1 nm bin. From these pooled data, hardness over a range of contact depth was calculated.

3. Results

To paint a comprehensive picture of the PLD growth of (TaNbHfTiZr)C, a systematic study was performed to optimize the surface composition, surface chemistry, and structure of the layers. The effect of the laser fluence F, background pressure of inert gas, the substrate material, and the deposition temperature on the surface composition were tested. These growth parameters determine the efficiency of material removal, transport, arrival, and mobility and thus provide multiple opportunities to influence the surface composition and chemistry measured by XPS.

Fig. 1 shows XPS spectra of a (TaNbHfTiZr)C film on $Al_2O_3(0001)$ acquired in the characteristic (a) Ta 4*d*, Nb 3*d*, Hf 4*d*, and Zr 3*d*, as well as (b) Ti 2*p*, and (c) C 1*s* regions, which were used for fitting and quantitative analysis. The observed binding energies are consistent with the formation of a metal carbide layer for all metals [45]. These specific regions were chosen to minimize and quantify overlaps between the different metal peaks and to reduce the effect of different electron kinetic energies on the probing depths.

The Ti $2p_{3/2}$ region is used as representative of the total titanium content because the Ti $2p_{1/2}$ region (464.5 eV) overlaps with the Zr 3*s* (466.5 eV) and Hf $4p_{1/2}$ (463 eV) regions. The implicit assumption that the intensity returns to background level between the Ti $2p_{3/2}$ and the Ti $2p_{1/2}$ peaks introduces a possible systematic underestimation of the Ti peak area. This effect is augmented by the lower kinetic energy of the Ti 2*p* electrons compared to other metal peaks. The reported values should thus be regarded as a lower limit of the Ti content. For the C 1*s* region, two species corresponding to carbon–carbon and carbon-metal bonds are fitted, which are indicated in Fig. 1(c). For spectra with a more pronounced high-energy tail, an additional species at 285.5 eV was fitted. The samples that were used for data analysis contain 5–10 atomic % oxygen, with higher average oxygen contents for depositions in Ne. At the highest oxygen contents, peak components corresponding to metal oxides are detected for Hf and Zr, indicating surface oxidation.

Effect of deposition fluence on surface composition

The laser fluence strongly affects the metal content of the resulting films and is an important parameter to consider when using a multi-elemental deposition target. Fig. 2 presents the surface composition of (TaNbHfTiZr)C films deposited on Si(100) with varying the fluence in UHV at room temperature. At low fluence, the film stoichiometry deviates strongly from the target composition. In particular the Ta content shows a strong dependence on fluence and depletion at low fluence values to less than 10% of all metals. Only above 10 J cm^{-2}, the Ta content becomes comparable to the other metals. Moreover, Fig. 2 shows the increase of Nb and a decrease in Hf and Ti with increasing fluence, whereas Zr remains constant within a variation of approximately ±1%. The equiatomic composition of the target is not

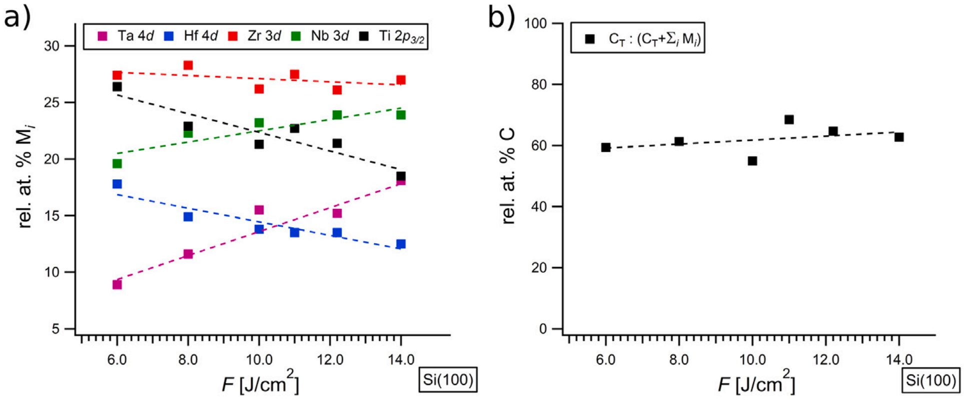

Fig. 2. Surface composition of (TaNbHfTiZr)C films as function of ablation fluence F in ultra-high vacuum ($p < 10^{-9}$ mbar) at room temperature. (a) Relative atomic concentration of individual metals normalized to total sum of metals. (b) Total carbon content normalized to the sum of carbon and all metals. Dashed lines serve as guide to the eye to illustrate the trends of surface composition of Ta, Hf, Zr, Nb, Ti and C as function of applied ablation fluence.

reached, but the fluence-dependence appears to decrease for values of 10 J cm^{-2} and above. In contrast to the variations observed for the metals, the evolution of the relative carbon content as a function of fluence, as seen in Fig. 2b, does not allow to derive any clear trend at UHV pressures at room temperature. Since depletion and enrichment of certain elements is reduced from 10 J cm^{-2}, this fluence was selected for the study of deposition pressure, substrate, and temperature.

Effect of Ne pressure on surface composition at room temperature

The effect of the deposition pressure on the surface composition of (TaNbHfTiZr)C layers was studied on two types of substrates, which differ in structure: Si(100) with a disordered native SiO_x layer and single-crystalline Al_2O_3(0001). Fig. 3 shows the surface composition as a function of the Ne background pressure during deposition. The data point at 10^{-9} mbar corresponds to the composition after deposition in UHV without process gas interactions. It should be remarked that the UHV-grown samples were prepared with a smaller number of shots (4500, ≈20 nm) and are thus expected to be thinner than the layers at finite Ne pressures (all 18 000 shots). The left column (a–c) corresponds to depositions on Si(100) while the right column (d–f) shows the results of depositions on Al_2O_3(0001) substrates. The trend lines in Fig. 3(a) and (d) reflect a similar evolution of the metal content in the surface region with Ne pressure for the two substrates. For increasing Ne pressures, the Hf and Ta content are found to increase whereas the Ti content decreases strongly. The Zr content decreases only weakly as function of Ne pressure and the Nb content remains approximately constant.

Similarly, the Ne pressure affects the final amount of carbon in the surface region, as shown in Fig. 3(b) and (e). Including the UHV reference composition, the relative atomic percentage of carbon with respect to the sum of carbon and metals varies between 42% and 64% for depositions on Si(100), and between 42% and 63% on Al_2O_3(0001). While the relative content of the total carbon peak (black dots) decreases with increasing Ne pressure, the relative contribution of the carbon species to the metal carbides (red dots) decreases only slightly, shifting to more metal-rich carbide compositions. It should be noted, however, that this apparently small decrease is reflected in a large change in the carbon stoichiometry x of the carbide MC_x. For the samples grown at room temperature on Al_2O_3(0001) substrates, this change corresponds to a drop from $x = 0.76$ to $x = 0.59$, which is approaching the limit of the typical equilibrium stability range of for example TiC_x [46].

The analysis of the carbon chemistry in Fig. 3(c), (f) show that the decrease in total carbon is reflected in an increase of the relative C 1*s* intensity stemming from metal-carbon (M–C) bonds (≈282.5 eV [45]) and the decrease of carbon–carbon (C–C) bonds (≈284.5 eV [45]) with increasing Ne pressure. The carbon–oxygen (C–O) bonds (≈285.5 eV) [47] increase slightly with increasing Ne pressure but do not significantly affect the observed trend.

Effect of the deposition temperature

In addition to Ne pressure, the substrate temperature is also shown to have a significant impact on the metal contents and the carbon composition. Only films grown on Al_2O_3(0001) were considered for the high-temperature study at 850 °C since at high growth temperatures we observed Si enrichment in the XPS data. Samples deposited at Ne pressures above 10^{-3} mbar are also not reported here, because they showed a strong enrichment in oxygen beyond the low-temperature values (<10%), distorting the metal and carbon composition of the surface region. In Fig. 3(d–f), the data for growth at 850 °C are marked by butterfly-shaped symbols and put in direct comparison to the otherwise equivalent room-temperature growth. The effect of substrate temperature on metal composition at the surface is visible in Fig. 3(d). The step to 850 °C introduces a clear enrichment in Ti in the surface region of the coating. The Zr and Nb contents decrease, whereas the effect on Ta and Hf is not consistent between the two different pressures. Interestingly, the total carbon content plotted in Fig. 3(e) changes significantly with the substrate temperature, approaching the nominal value for a stoichiometric rocksalt (TaNbHfTiZr)C of 50%. At the same time, the total carbon content aligns closely with the carbon content attributed to the carbide particles. This observation is also reflected in Fig. 3(f), which shows very low or no C 1*s* intensity at 284.5 eV for the high-temperature depositions, in stark contrast to room-temperature samples.

Effect of PLD parameters on structure

To assess the effect of deposition pressure and substrate temperature on the structure of PLD-grown (TaNbHfTiZr)C, *ex-situ* GIXRD and SEM were performed on selected samples of the set shown in Fig. 3. Fig. 4 shows integrated diffractograms (a) calculated from two-dimensional GIXRD patterns (b) for (TaNbHfTiZr)C deposited on Al_2O_3(0001) at three different deposition conditions: 10^{-3} mbar Ne at room temperature (Sample HEC-RT-3Ne), 10^{-3} mbar Ne at 850 °C (Sample HEC-850-3Ne), and UHV at 850 °C (Sample HEC-850-UHV). The integration of the 2D GIXRD intensity is performed along rings of constant diffraction angle within a pre-selected integration area, indicated by the blue lines in Fig. 4(b).

For all three samples, the diffractograms in Fig. 4 are consistent with a rocksalt carbide structure. Based on setup-dependent uncertainties in the sample alignment, a large error bar must be considered when

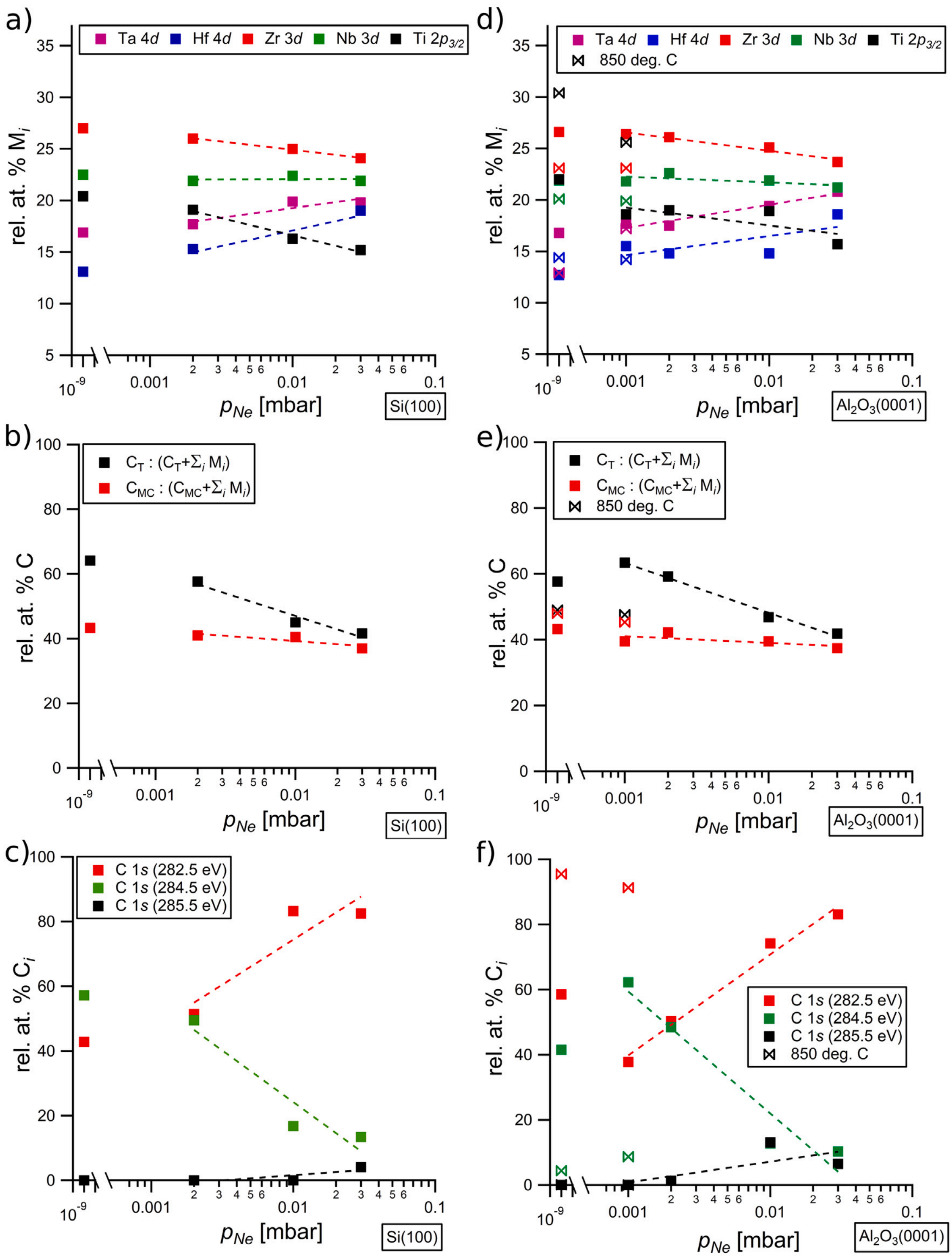

Fig. 3. Surface composition of (TaNbHfTiZr)C films as function of deposition pressure in Ne gas (p_{Ne}), deposited on Si(100) (a–c) and Al_2O_3(0001) (d–f). (a,d) Relative atomic concentration of individual metals. (b,e) Relative atomic concentration of total carbon (black) and carbide-like carbon (red) with respect to total sum of carbon and metals. (c,f) Relative concentration of carbon species at binding energies of 282.5 eV, 284.5 eV and 285.5 eV, representing M–C, C–C and C–O bond content, respectively. Dashed lines serve as guide to the eye illustrating the trends of surface composition of Ta, Hf, Zr, Nb, Ti, and C species as function of Ne pressure during deposition. Butterfly-shaped data points in (d–f) show surface composition of metals and carbon grown at 850 °C.

estimating the lattice parameter from the diffraction angles. The approximated lattice constant of 0.45 ± 0.03 nm is consistent with typical values for refractory metal carbides. Larger variations than 0.03 nm are considered unlikely, because the corresponding variation in angle should lead to the presence of stronger substrate signals in GIXRD. To facilitate comparison of the relative peak positions between samples, diffractogram (1) is shifted to match the (111) peak of the two other samples. At high diffraction angles a small difference remains ($\Delta 2\theta < 0.5°$), indicating small differences in the (average) lattice constants of less than 0.6%. The peak width and two-dimensional intensity distributions, however, vary substantially between samples. In particular the sample deposited at room temperature in 10^{-3} mbar Ne exhibits

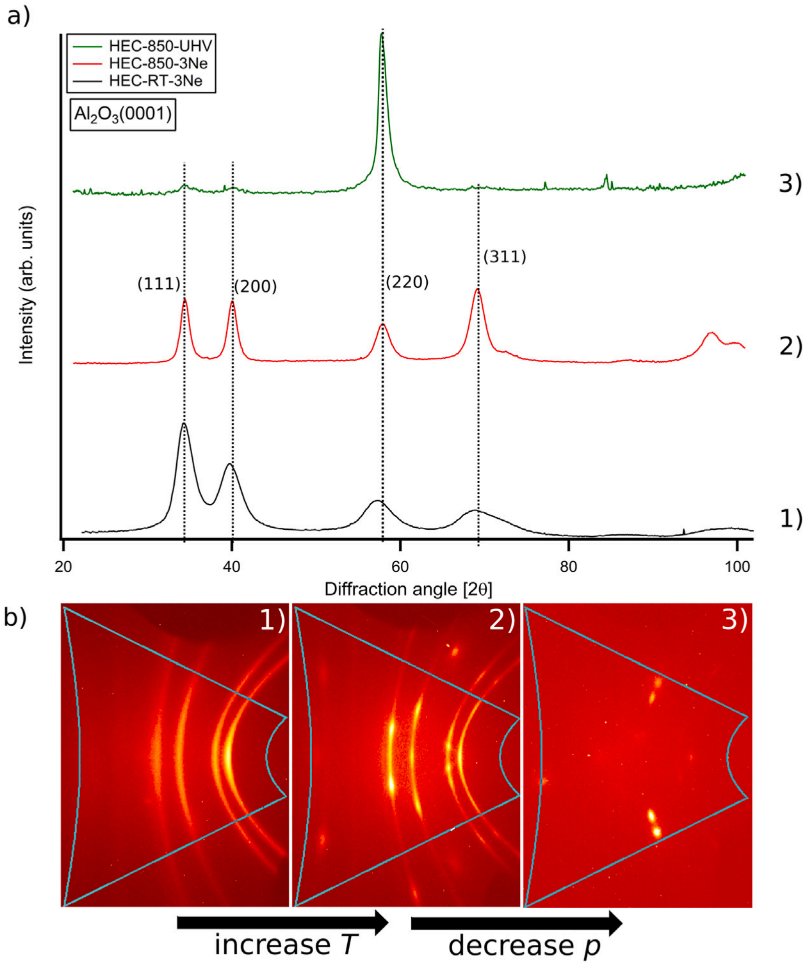

Fig. 4. GIXRD measurements on (TaNbHfTiZr)C on $Al_2O_3(0001)$. (a) Integrated GIXRD signal of HEC-RT-3Ne grown at room temperature in 10^{-3} mbar Ne (1), HEC-850-3Ne grown at high temperature (850 °C) in 10^{-3} mbar Ne (2) and HEC-850-UHV, grown at high temperature in ultra-high vacuum (3). Setup-dependent uncertainty in sample alignment results in shifts in the absolute peak position. Curve (a.1) was shifted by 1.98 degrees to align to the (111) peak position of others to facilitate comparison and show that the differences in relative peak position are small. The original data is shown as dashed line. (b) Corresponding 2D detector images. The integration areas used to obtain the diffractograms in (a) are indicated as blue regions.

wider diffraction peaks than the high-temperature samples, indicating either smaller particle sizes or the coexistence of carbide grains with different lattice constants. In a coarse approximation attributing the full broadening to size effects, the average grain sizes were calculated from the peak shapes of the main diffraction peaks corresponding to the (111), (200) and (220) planes. The calculated values show a trend of increasing crystallinity at higher temperature, with approximate grain sizes of 3 nm for HEC-RT-3Ne, 6 nm for HEC-850-3Ne, and 7.4 nm for HEC-850-UHV. The suppressed (111) and (200) peaks for HEC-850-UHV were not taken into account for this estimate. The different peak intensities for different growth conditions and the changes in peak shapes further indicate changes in orientational preference and possible strain effects.

More detailed information on these structural properties can be obtained from the 2D diffractograms in 4(b). The sample HEC-RT-3Ne yields a 2D diffraction pattern with rings of continuous intensity at well-defined angles that is characteristic of randomly oriented polycrystalline layers, as shown in Fig. 4(b.1). The pattern of HEC-850-3Ne in Fig. 4(b.2) shows a superposition of rings and spots at well-defined angles, indicating the coexistence of both randomly oriented crystallites and grains that retain a specific orientation with respect to the $Al_2O_3(0001)$ substrate. Finally, the elevated temperature growth in UHV (HEC-850-UHV) shows only diffraction spots with no indication of rings, demonstrating crystallinity and a strong orientational preference with respect to the substrate. The strongest features in the pattern occur as double spots close to $2\theta = 58°$, the angle characteristic of the (220) plane. The coexistence of two spots with different shapes and positions results in the peak asymmetry of the (220) reflection in the integrated diffractogram. SEM micrographs of the same three samples (Supporting Information, Figures S1–S3) confirm the trend observed in diffraction, with a general increase in order, homogeneity, and particle size at high temperature. In particular the images of HEC-850-UHV in Figure S3 show a dense arrangement of crystallites without signs of coexistence with a second phase.

Nanoindentation results

According to the XPS and XRD results, the high-temperature growth of (TaNbHfTiZr)C produces oriented HEC layers with a rocksalt structure in the preferred carbon stoichiometry range of refractory carbides, which may reflect the promising properties of bulk HECs. To connect the properties of these optimized PLD-grown layers to potential applications as functional coatings, the hardness of an approximately 600 nm thick (TaNbHfTiZr)C film grown on $Al_2O_3(0001)$ at 850 °C in UHV (HEC-850-UHV-thick) was measured using nanoindentation. Fig. 5 presents the hardness as a function of indentation depth of the (TaNbHfTiZr)C/$Al_2O_3(0001)$ coating. The square markers represent the mean hardness of the (TaNbHfTiZr)C coating at the respective contact depth, with their standard deviation as error bar. The red and blue

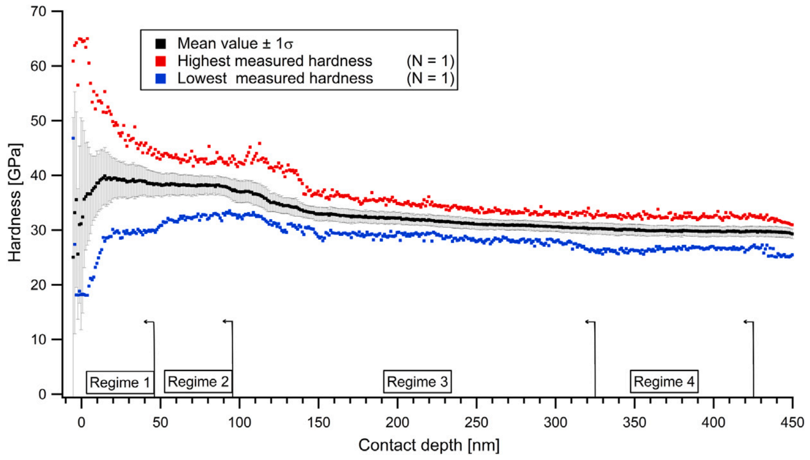

Fig. 5. Nanoindentation of (TaNbHfTiZr)C/Al_2O_3(0001) grown at 850 °C in UHV (HEC-850-UHV-thick). Four regimes are discernible in the measurement. Regime 1: initial regime at low indentation depth, where the area function is ill-defined, yielding unreliable hardness values. Regime 2: plateau regime dominated by the response of the (TaNbHfTiZr)C coating. Regime 3: mixed regime in which the measured hardness decreases with increasing contact depth. We interpret the reduction in measured hardness with contact depth as a result of the growing contribution of the deformations of the sapphire substrate to the indentation measurement. Regime 4: substrate-dominated regime. A representative hardness of the (TaNbHfTiZr)C coating was calculated from the mean hardness and corresponding standard deviation between 45–95 nm contact depth.

markers represent the highest and lowest hardness values measured at every contact depth bin. The average mean and pooled standard deviation for the data in regime 2 (45–95 nm contact depth) provide an average hardness of the sample of 38.3 GPa ± 1.9 GPa. In regimes 3 and 4, the measured value decreases and approaches the hardness of the substrate, in agreement with a reference measurement performed on the same setup [35] on bare Al_2O_3(0001) substrate (Supporting Information, Figure S4), where a hardness of 28 GPa ± 1 GPa was measured.

4. Discussion

The chemical and structural data on pulsed-laser-deposited (TaNbHfTiZr)C demonstrate the successful growth of a single-phase HEC layer. The PLD parameters fluence, inert gas pressure, and substrate temperature are found to significantly affect the carbon and metal stoichiometry of (TaNbHfTiZr)C as well as their structure. The data further shows that the transfer from the equiatomic target does not fully conserve stoichiometry, but the composition can be controlled towards near-equiatomic metal composition and near-stoichiometric metal-to-carbon content. Importantly, the inert gas pressure and substrate temperature also strongly influence the carbon chemistry of the layer from a mixture of carbide grains and elemental carbon to films showing almost exclusively carbide-like bonds.

The first deposition parameter under study, the laser fluence, was found to strongly influence the composition of the resulting films. The most prominent changes in Fig. 2 are a strong increase of Ta content and strong decrease of Ti content with increasing fluence. These relative changes in metal content are attributed to a combined effect of ablation efficiency of the mixture of binary carbides in the target [48] and resputtering at the deposition substrate [49]. All fluences in Fig. 2 are clearly above the ablation thresholds for the individual carbides. Above the threshold, the ablation rate of most refractory metal carbides is expected to increase linearly with the laser fluence [32,50]. TiC forms an exception, showing a flat dependence on fluence in the range of 4–8 J cm^{-2}, followed by an accelerated increase at higher fluences [50]. Since this is contrary to a decrease in Ti content at the highest fluences studied here, we propose that this effect is more likely due to the preferential removal of the lightest metal Ti upon an increase in the average ion energy in the plasma plume at higher fluences. This mechanism, however, does not explain the decrease of the Hf content, which is most pronounced at the lower fluences and relatively flat at higher values. Alternative explanations could be a varying slope of the fluence-dependent deposition rate of the different metals, preferential oxidation of Hf, or a different sticking of higher-energy species that are produced in the plume at increasing fluence. The weakly varying carbon content suggests that in the studied fluence range, there are no systematic changes in the stoichiometric transfer of carbon. In the surface region probed by XPS the carbon content remains close to 60%. While the distribution among the individual carbon species was not analyzed in the fluence-dependent study, the UHV deposition in Fig. 3(c) indicates that a significant part of the “excess” carbon is present in the form of elemental carbon at comparable growth conditions.

The second parameter, the background pressure of inert gas in the chamber during deposition, also has a systematic effect on the metal ratios and the carbon content, as illustrated in Fig. 3. Increasing the Ne pressure results in a systematic trend of decreasing Ti and C signals whereas the contents of Hf and Ta increase. These trends correlate well with the atomic mass of the elements, with C and Ti being the lightest two elements and Hf and Ta the heaviest ones in the deposition plasma. The masses of the elements play an important role in the scattering with the Ne process gas, with lower masses resulting in larger scattering angles and energy changes after single scattering events. This causes an increased probability for heavier elements to reach the substrate and can lead to an enrichment of Hf and Ta. In addition to this effect, reactive elements like Hf may also enrich due to oxidation at increasing pressures and thus increasing levels of oxidizing contaminants. However, the depletion of Zr at increasing Ne pressures indicates that this chemically induced change in surface composition contributes less than the scattering with Ne. In addition to the metals, carbon also undergoes scattering in the gas. Since carbon is even lighter than Ne, a ballistic collision with central impact on Ne will result in backscattering and high scattering angles are expected for a wide range of collisions. The presence of high Ne pressures thus introduces a high probability for carbon atoms to miss the deposition substrate entirely. This effect is expected to cause the substantial decrease in carbon content for high Ne pressures, consistent with the trend reported in Fig. 3(c) and (f).

In addition to the elemental composition, also the chemical nature of the carbon species at the surface undergoes a systematic change with Ne pressure. Specifically, the contribution of carbon–carbon bonds drops steeply as the Ne pressure increases, while the carbon content of the HEC grains decreases mildly. This observation indicates that lower supply of carbon due to scattering preferentially affects the content of elemental carbon but also increases the level of carbon-deficiency in the carbide lattice. The results at low Ne pressure indicate that the room-temperature samples are still far from stoichiometric ($MC_{0.76}$) even if enough carbon is supplied. We attribute this effect to the low mobility at room temperature, which hinders diffusion, as well as the large stability range in the metal-carbon phase diagrams of refractory metal carbides [31,46]. A similar interpretation of carbon-deficient (TaNbHfTiZr)C with a secondary phase of excess carbon has been reported for sputter-deposited layers already for low supply of excess carbon [31]. This is in line with the phase diagram for several refractory carbides, which tend to form embedded carbide particles in a carbon matrix for carbon-rich stoichiometries [8,51,52], which is a possible interpretation of the featureless regions between grains in the SEM images of HEC-RT-3Ne and HEC-850-3Ne. The presence of elemental carbon may also be related to the presence of high-energy species in the plasma plume, which can introduce disorder by damaging carbide particles when impinging on the surface. Since a substrate at room temperature does not supply sufficient energy for significant mobility of atoms at the surface, this may lead to a higher content of carbon outside the carbide lattice. A lower average energy of the plasma components with increasing Ne pressure may thus decrease the level of disorder at the surface and offer an explanation of the lower content of carbon–carbon bonds, complementary to a preferred carbon deficient stoichiometry.

The deposition temperature shows a distinct effect on composition, chemistry, and structure for the two pressure regimes studied (UHV and low Ne pressure, both at 850 °C). In Fig. 3(d–f), the high-temperature data points are directly compared to the low-temperature growth series. The most striking difference between metal content at room temperature and 850 °C is the Ti enrichment at the higher growth temperature for both environments. While the incoming flux of material is not expected to change significantly as a function of substrate temperature and an enhanced sticking specifically for Ti is unlikely, the elevated temperature is expected to enhance the mobility of atoms during the growth. Already for average diffusion distances in the nanometer range, this is expected to enable the enrichment of low-surface-energy materials in the surface region. A comparison of the reported surface energies of the five binary carbides of Hf, Nb, Ta, Ti, and Zr, yields the lowest value for titanium carbide [53,54]. The material is thus driven to terminate the HEC film with a Ti-rich layer, which will result in a significant increase of the XPS intensity of Ti and mimic a Ti-rich layer.

Also the carbon chemistry of the layer is substantially affected by the temperature. Already the total carbon content undergoes a substantial change with the increase in deposition temperature to 850 °C, decreasing to 49% and thus closely approaching the nominal stoichiometry of the target. The relative contribution of the carbidic carbon species, on the other hand, increases to more than 95% of the total carbon, indicating that the layer consists almost exclusively of carbide grains. The composition of the carbide phase becomes closer to stoichiometric, $MC_{0.92}$, showing a significantly improved uptake of carbon to the carbide phase. This trend is comparable for the high-temperature growth in UHV and in 10^{-3} mbar Ne (HEC-850-UHV and HEC-850-3Ne), with more carbon deficiency at higher pressure. The substantial difference to the room-temperature depositions, which result in the growth of a carbon-depleted layer and the accumulation of residual carbon, is the mobility of atoms in the surface region at high temperature.

The information on the carbon species from XPS data is useful to combine with structural data from the diffraction patterns and SEM images. The increase in temperature strongly changes the diffraction features from continuous broad rings to patterns dominated by spots at well-defined angles. In comparison to the low-temperature case of HEC-RT-3Ne, the sample HEC-850-3Ne grown at elevated pressure and temperature produces narrower rings that coexist with a small number of sharp diffraction spots. This difference indicates the emergence of an orientational preference in the polycrystalline layer and an increased crystallite size, in agreement with the observation of larger grains of well-defined shape in the SEM images of the high-temperature samples. Decreasing the deposition pressure at high temperature results in an even stronger orientational preference, indicated by the formation of sharp spots without significant background intensity or ring-like features for HEC-850-UHV. In SEM images, this is observed as a dense arrangement of grains without regions of low contrast in between. According to the diffraction results, the crystallites converge to one orientation, preferentially aligning one type of crystal plane with the substrate. The sapphire (0001) surface and the (111) plane of the rock-salt carbide are the most intuitive fit, with a good match of the in-plane lattice constants $a_{\mathrm{Al2O3(0001)}} \approx 1.5 \times a_{HEC(111)}$. The observation of the (111) reflection in the center of the 2D diffraction patterns shows that a plane of this type fulfills the conditions for out-of-plane diffraction. Interestingly, the (220) spot emerges as the strongest feature in the integrated diffractograms. It should, however, be noted that it is not in the center of the diffraction pattern and would not even be detected for a $\theta/2\theta$ scan with a line detector. Diffraction at this solid angle thus requires a vector with a significant in-plane component, which originates from the inclination of the respective cubic planes to the surface plane. The increased intensity of the (220) diffraction spot indicates that many grains are aligned the same way and allow for a symmetric reflection of the incoming beam from the respective planes, which in GIXRD is not possible for planes parallel to the surface. For a randomized arrangement of grains, all orientations with respect to the surface normal are represented and all planes have strong contributions to the diffraction rings in the 2D diffractograms.

While the increasing order at higher temperature is clearly related to enhanced mobility, the explanation of the increasing order at lower Ne pressure at high temperature is less obvious. A possible origin for this more strongly oriented growth at low pressures may be the higher energies of impinging particles, which damage the growing crystallites. While this effect would lead to more disorder at low temperature, the increased mobility at 850 °C is expected to help repair the damage, favoring the lowest-energy structures of the layer. Thus, if a specific orientation with respect to the substrate lowers the energy, it will have an even higher chance of forming. The splitting of the diffraction spots of this ordered layer (in Fig. 4(b.3)) is interpreted as a sign that the epitaxial match with the Al_2O_3(0001) substrate is not perfect, but results in two types of domains.

The trends in composition and structure illustrate the potential of PLD for the optimization of thin-film properties. The result of the growth is tunable by the parameters and ranges from HEC crystallites coexisting with elemental carbon to single-phase HEC coatings. From a perspective of high-entropy materials, the carbide layer grown at 850 °C comes closest to single-phase equiatomic (TaNbHfTiZr)C. This sample was thus selected to test an application-oriented materials property for coatings, the film hardness. The measured hardness value of 38.3 ± 1.9 GPa is in agreement with values from the literature, exceeding that of sputter-deposited layers [24,31] and approaching the highest hardnesses of bulk (TaNbHfTiZr)C [20,23,26,55]. This high hardness is in line with the reported hardness enhancement for of thin films [56] and nanocrystalline materials [57], while also exceeding the hardness measured for PLD-deposited binary carbides [1,33]. The HEC layer with the optimized structure thus surpasses the expectations of mixing refractory metal carbides and thin HEC films, approaching the regime of superhard coatings.

5. Conclusion

In conclusion, we show that using PLD, thin films of single-phase rock-salt (TaNbHfTiZr)C high-entropy carbide can be produced with superior hardness compared to other deposition techniques. Our systematic PLD growth study of (TaNbHfTiZr)C on Si(100) and Al_2O_3(0001)

reveals the potential of the growth parameters to tune surface composition and structure of the coatings. The effects of fluence on surface composition in UHV show that its variation allows for steering the ratio of light to heavy metals whilst leaving the carbon stoichiometry practically unaffected. The Ne pressure during deposition, conversely, affects both the content of metals and carbon via stronger scattering of light elements and lowering the energy of the deposition plasma species. The stoichiometry of the metal carbide phase MC_x itself is highly sensitive to changes in deposition temperature and varied between 0.6 and 0.92, with the highest values achieved for deposition at 850 °C. The tunability of the composition and structure achieved with PLD provides access to customized coatings ranging from hard single-phase HECs to carbide grains coexisting with a phase of elemental carbon. The hardness of the single-phase coating is found to be 38 GPa, approaching the hardest HECs reported in the literature. While the single-phase layer HEC-850-UHV is closest to the theoretical structure and composition of pure (TaNbHfTiZr)C, even higher hardness values may be achievable by varying the structure and stoichiometry. Exploring the hardness as a function of composition and crystallinity as well as the toughness and wear-resistance of these layers are considered promising opportunities for future research on the application of high-performance HECs as thin film coatings.

CRediT authorship contribution statement

Tadeus Nikos Hogenelst: Writing – original draft, Visualization, Investigation, Formal analysis, Data curation. **Cyrian Leriche:** Writing – original draft, Investigation, Formal analysis, Data curation. **Alessandro Troglia:** Writing – review & editing, Methodology, Investigation. **Bart Weber:** Writing – review & editing, Supervision, Resources. **Roland Bliem:** Writing – review & editing, Writing – original draft, Validation, Supervision, Project administration, Funding acquisition, Formal analysis, Conceptualization.

Funding

This work was conducted at the Advanced Research Center for Nanolithography, a public–private partnership between the University of Amsterdam (UvA), Vrije Universiteit Amsterdam (VU), Rijksuniversiteit Groningen (RUG), the Netherlands Organization for Scientific Research (NWO), and the semiconductor equipment manufacturer ASML.

Declaration of competing interest

The authors declare that they have no known competing financial interests or personal relationships that could have appeared to influence the work reported in this paper.

Acknowledgments

We thank Dr. Sven Hennig (Vrije Universiteit) for the support in the GI-XRD measurements and Dr. Anna Isaeva (University of Amsterdam) for providing valuable discussion and interpretation of the GIXRD data. Furthermore we thank Joost Frenken for providing insight at an early stage of the research and Wim van der Zande for providing valuable feedback during later stages of the research.

Appendix A. Supplementary data

Supplementary material related to this article can be found online at https://doi.org/10.1016/j.surfcoat.2025.132976.

Data availability

Data will be made available on request.

References

[1] S.M. Barinov, D. Ferro, C. Bertuli, L. D'Alessio, J. Mater. Sci. Lett. 20 (2001) 1485–1487.
[2] Y. Liu, Y. Jiang, R. Zhou, J. Feng, J. Alloys Compd. 582 (2014) 500–504.
[3] E. Castle, T. Csanádi, S. Grasso, J. Dusza, M. Reece, Sci. Rep. 8 (2018) 8609.
[4] G. Wang, J. Xu, S. Peng, Z. Xie, P. Munroe, Vacuum 211 (2023) 111974.
[5] Y.L. Krutskii, T.S. Gudyma, I.D. Kuchumova, R.R. Khabirov, K.A. Antropova, Steel Transl. 52 (2022) 465–478.
[6] Y.V. Stulov, V.S. Dolmatov, A.R. Dubrovskii, S.A. Kuznetsov, Russ. J. Appl. Chem. 90 (2017) 676–683.
[7] P. Montenegro, J. Gomes, R. Rego, A. Borille, IJRMHM 70 (2018) 116–123.
[8] E. Lewin, U. Jansson, Thin Solid Films 536 (2013) 1–24.
[9] K. Balasubramanian, S.V. Khare, D. Gall, Acta Mater. 152 (2018) 175–185.
[10] Z. Shi, E. Tsymbalov, W. Shi, A. Barr, Q. Li, J. Li, X. Chen, M. Dao, S. Suresh, J. Li, Proc. Natl. Acad. Sci. USA 121 (2024) e2313840121.
[11] C.H. de Novion, B. Beuneu, T. Priem, N. Lorenzelli, A. Finel, Defect Structures and Order-Disorder Transformations in Transition Metal Carbides and Nitrides, first ed., Kluwer Academic Publishers, 1990.
[12] C.H. de Novion, J.P. Landesman, Pure Appl. Chem. 57 (1985) 1391–1402.
[13] W. Sun, H. Ehteshami, P.A. Korzhavyi, Phys. Rev. B 91 (2015) 1–11.
[14] Q.H. Zhao, J. Wu, A.K. Chaddha, H.S. Chen, J.D. Parsons, D. Downham, J. Mater. Res. 9 (1994) 2096–2101.
[15] Y. Zhou, G. Fahrenholtz, J. Graham, G.E. Hilmas, J. Mater. Sci. Technol. 82 (2021) 105–113.
[16] E. Lewin, M. Råsander, M. Klintenberg, A. Bergman, O. Eriksson, U. Jansson, Chem. Phys. Lett. 496 (2010) 95–99.
[17] W. Zhang, K. Li, L. Chen, Z. Shi, S. Huo, B. Wei, S. Kang, Y. Wang, Y. Zhou, J. Eur. Ceram. Soc. 44 (2024) 1396–1403.
[18] C. Oses, C. Toher, S. Curtarolo, Nat. Rev. Mater. 5 (2020) 295–309.
[19] J.-W. Yeh, S.-K. Chen, S.-J. Lin, J.-Y. Gan, T.-S. Chin, T.-T. Shun, C.-H. Tsau, S.-Y. Chang, Adv. Eng. Mater. 6 (2004) 299–303.
[20] T.J. Harrington, J. Gild, P. Sarker, C. Toher, C.M. Rost, O.F. Dippo, C. McElfresh, K. Kaufmann, E. Marin, L. Borowski, P.E. Hopkins, J. Luo, S. Curtarolo, D.W. Brenner, K.S. Vecchio, Acta Mater. 166 (2019) 271–280.
[21] Q. Zhang, J. Zhang, N. Li, W. Chen, J. Appl. Phys. 126 (2019) 025101.
[22] E.P. George, D. Raabe, R.O. Ritchie, Nat. Rev. Mater. 4 (2019) 515–534.
[23] P. Sarker, T. Harrington, C. Toher, C. Oses, M. Samiee, J.-P. Maria, D.W. Brenner, K.S. Vecchio, S. Curtarolo, Nat. Commun. 9 (1) (2018) 4980.
[24] V. Braic, A. Vladescu, M. Balaceanu, C. Luculescu, M. Braic, Surf. Coat. Technol. 211 (2012) 117–121, Proceedings of Symposium K on Protective Coatings and Thin Films, E-MRS 2011 Conference.
[25] P.-X. Zhang, L. Ye, F.-H. Chen, W.-J. Han, Y.-H. Wu, T. Zhao, J. Alloys Compd. 903 (2022) 163868.
[26] B. Ye, T. Wen, K. Huang, C.-Z. Wang, Y. Chu, J. Am. Ceram. Soc. 102 (7) (2019) 4344–4352.
[27] L. Daková, M. Hrubovcáková, A. Kovalcíková, D. Medved, J. Andrejovská, F. Kromka, L. Medvecký, J. Dusza, Int. J. Refract. Met. Hard Mater. 119 (2024) 106549.
[28] H. Chen, H. Xiang, F. Dai, J. Liu, Y. Lei, J. Zhang, Y. Zhou, J. Mater. Sci. Technol. 35 (2019) 1700–1705.
[29] Q. Yang, C. Li, H. Ouyang, R. Gao, T. Shen, J. Huang, Mater. 16 (6) (2023) 2495.
[30] J. Zhou, J. Zhang, F. Zhang, B. Niu, L. Lei, W. Wang, Ceram. Int. 44 (17) (2018) 22014–22018.
[31] M.D. Hossain, T. Borman, A. Kumar, X. Chen, A. Khosravani, S.R. Kalidindi, E.A. Paisley, M. Esters, C. Oses, C. Toher, S. Curtarolo, J.M. LeBeau, D. Brenner, J.-P. Maria, Acta Mater. 215 (2021) 117051.
[32] L. D'Alessio, A. Galasso, A. Santagata, R. Teghil, A. Villani, P. Villani, M. Zaccagnino, Appl. Surf. Sci. 208–209 (2003) 113–118, Physics and Chemistry of Advanced Laser Materials Processing.
[33] D. Ferro, J.V. Rau, V. Rossi Albertini, A. Generosi, R. Teghil, S.M. Barinov, Surf. Coat. Technol. 202 (8) (2008) 1455–1461.
[34] A. Salian, S. Mandal, Bull. Mater. Sci. 45 (2022) 49.
[35] A. Troglia, C. Leriche, M.L. van de Poll, C. Morscher, G.H. ten Brink, B.J. Kooi, B. Weber, R. Bliem, Mater. Today Commun. 41 (2024) 110604.
[36] J. Brecht, P.K. Liaw, High-Entropy Materials: Theory, Experiments, and Applications, Springer Nature, 2021.
[37] M.V. Kante, M.L. Weber, S. Ni, I.C. van den Bosch, E. van der Minne, L. Heymann, L.J. Falling, N. Gauquelin, M. Tsvetanova, D.M. Cunha, et al., ACS Nano 17 (6) (2023) 5329–5339.
[38] M.V. Kante, H. Hahn, S.S. Bhattacharya, L. Velasco, J. Alloys Compd. 947 (2023) 169430.
[39] J. Woo, Growth of Epitaxial Zirconium Carbide Layers Using Pulsed Laser Deposition (PhD dissertation), University of Florida, 2005.
[40] J. Végh, J. Electron Spectrosc. Relat. Phenom. 151 (2006) 159–164.
[41] S.A. Hassanzadeh-Tabrizi, J. Alloys Compd. 968 (2023) 171914.
[42] W.C. Oliver, G.M. Pharr, J. Mater. Res. 19 (2004) 1–20.
[43] W.C. Oliver, G.M. Pharr, J. Mater. Res. 7 (1992) 1563–1583.
[44] R. Saha, W.D. Nix, Acta Mater. 50 (2002) 23–38.

[45] G. Greczynski, D. Primetzhofer, L. Hultman, Appl. Surf. Sci. 436 (2018) 102–110.

[46] H. Okamoto, J. Phase Equilib. 16 (6) (1995) 532–533.

[47] W.H. Lee, J.G. Lee, P.J. Reucroft, Appl. Surf. Sci. 171 (1–2) (2001) 136–142.

[48] N.A. Shepelin, Z.P. Tehrani, N. Ohannessian, C.W. Schneider, D. Pergolesi, T. Lippert, Chem. Soc. Rev. 7 (2023) 2294–2321.

[49] K. Sturm, H. Krebs, J. Appl. Phys. 90 (2001) 1061–1063.

[50] R. Teghil, L. D’Alessio, M. Zaccagnino, D. Ferro, V. Marotta, G. De Maria, Appl. Surf. Sci. 173 (3) (2001) 233–241.

[51] N. Nedfors, O. Tengstrand, E. Lewin, A. Furlan, P. Eklund, L. Hultman, U. Jansson, Surf. Coat. Technol. 206 (2011) 354–359.

[52] M. Magnuson, E. Lewin, L. Hultman, U. Jansson, Phys. Rev. B 80 (2009) 235108.

[53] E.N. Eremin, V.M. Yurov, V.C. Laurynas, S.A. Guchenko, S.S. Kasymov, J. Phys.: Conf. Ser. 1210 (1) (2019) 012041.

[54] H. Hugosson, O. Eriksson, U. Jansson, A. Ruban, P. Souvatzis, I. Abrikosov, Surf. Sci. 557 (1) (2004) 243–254.

[55] J. Dusza, T. Csanádi, D. Medved, R. Sedlák, M. Vojtko, M. Ivor, H. Ünsal, P. Tatarko, M. Tatarková, P. Šajgalík, J. Eur. Ceram. Soc. 41 (11) (2021) 5417–5426.

[56] D. Ferro, R. Teghil, S.M. Barinov, L. D’Alessio, G. DeMaria, Mater. Chem. Phys. 87 (2004) 233–236.

[57] M. Meyers, A. Mishra, D. Benson, Prog. Mater. Sci. 51 (4) (2006) 427–556.